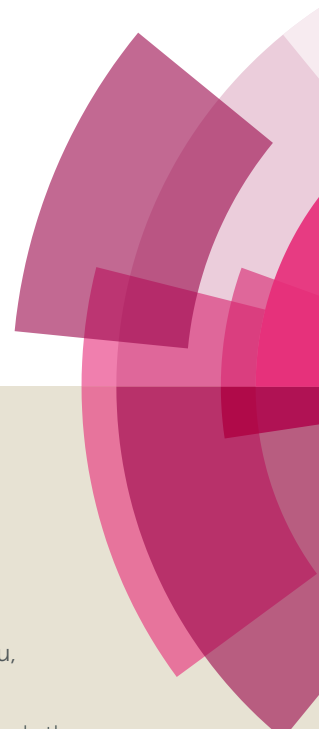


NJC

Accepted Manuscript



This article can be cited before page numbers have been issued, to do this please use: S. Zheng, K. Zhu, W. Li and Y. Ji, *New J. Chem.*, 2017, DOI: 10.1039/C6NJ03960J.



This is an Accepted Manuscript, which has been through the Royal Society of Chemistry peer review process and has been accepted for publication.

Accepted Manuscripts are published online shortly after acceptance, before technical editing, formatting and proof reading. Using this free service, authors can make their results available to the community, in citable form, before we publish the edited article. We will replace this Accepted Manuscript with the edited and formatted Advance Article as soon as it is available.

You can find more information about Accepted Manuscripts in the [author guidelines](#).

Please note that technical editing may introduce minor changes to the text and/or graphics, which may alter content. The journal's standard [Terms & Conditions](#) and the ethical guidelines, outlined in our [author and reviewer resource centre](#), still apply. In no event shall the Royal Society of Chemistry be held responsible for any errors or omissions in this Accepted Manuscript or any consequences arising from the use of any information it contains.



Journal Name

ARTICLE

Hydrogenation of Dimethyl Malonate to 1,3-Propanediol Catalyzed by Cu/SiO₂ Catalyst: Reaction Network and Effect of Cu⁺/Cu⁰ on Selectivity

Sainan Zheng^a, Kake Zhu^a, Wei Li^{a*}, and Yang Ji^b

Received 00th January 20xx,
Accepted 00th January 20xx

DOI: 10.1039/x0xx00000x

www.rsc.org/

Abstract: 1,3-propanediol, a vital monomer for the manufacture of commodity poly trimethylene-terephthalate, is commercially produced nowadays through either hydration of acrolein or hydroformylation of ethylene oxide. Herein, for the first time, we present the investigation of an alternative route for 1,3-propanediol production from vapor-phase catalytic hydrogenation of syngas-derived dimethyl malonate on Cu/SiO₂ catalyst. The catalytic reaction network has been disclosed for Cu/SiO₂ catalyst, the reaction proceeds through sequential hydrogenation with methyl 3-hydroxypropionate as the primary product, which can be further converted into 1,3-propanediol or methyl propionate. Excessive hydrogenation of 1,3-propanediol or methyl propionate leads to the formation of n-propanol. Meanwhile, a small amount of dimethyl malonate cracks into methyl acetate. The structural and textural properties of Cu/SiO₂ catalysts with varied copper loadings were extensively characterized by X-ray diffraction, Fourier transform infrared spectroscopy, H₂-temperature programmed reduction, X-ray photoelectron spectroscopy, N₂ physisorption, CO chemisorption, N₂O titration, and transmission electron microscopy. A correlation of areal activity to copper components suggests that metallic copper modified by the co-present Cu⁺ specie may be the active site for the hydrogenation. The highest 1,3-propanediol selectivity was achieved on a catalyst with maxima Cu⁺/(Cu⁰+Cu⁺) ratio of 0.41. The revelation of catalytic network and insight into the active species can provide guidance for future rational design of catalysts for regioselective hydrogenation of C=O bonds in dimethyl malonate.

Keywords: dimethyl malonate, 1,3-propanediol, vapor-phase hydrogenation, Cu⁰/Cu⁺ active sites, synergetic effect

1. Introduction

Poly trimethylene-terephthalate (PTT) is an attractive polymer which finds broad applications in fiber and textile industries due to its better stretching and stretch-recovering characteristics, lower dyeing temperature, and higher light stability than other polyesters. In particular, its biodegradability offers great competitive environmental and economic advantages.^{1,2} One of the monomer for PTT, 1,3-propanediol (1,3-PDO), is nowadays produced chiefly via two routes: hydration of acrolein by the Degussa process and hydroformylation of ethylene oxide by the Shell process.³ Besides, microbial production has recently been reported as an alternative for 1,3-PDO synthesis.⁴⁻⁶ Moreover, hydrogenolysis of glycerol also potentially contributes the commercial productivity of 1,3-PDO.⁷⁻⁹ Recently, Ding et al. reported another approach to synthesize 1,3-PDO involving hydrogenation of diethyl malonate.^{10,11} Since the global market for PTT production is predicted to rise continuously, the gap

between production and the global market will widen progressively.¹² Therefore, there is a driven force to cultivate other ways to meet the increasing demand for 1,3-PDO production. Dimethyl malonate (DMM) hydrogenation to 1,3-PDO is a possible alternative route for large scale production, as DMM can potentially be generated from both syngas- and petroleum-derived products, for instance, via carbonylation of dihalo methane and carbonylation of methyl chloroacetate.^{13,14} More importantly, DMM can be synthesized via a Claisen condensation process involving methyl carbonate and dimethyl carbonate, both of which are commercially produced through low-cost syngas-based routes. This approach for preparing DMM has been investigated in our previous work.¹⁵ In this contribution, DMM hydrogenation to 1,3-PDO via a vapor-phase catalytic process over a Cu/SiO₂ catalyst is tentatively explored.

Copper-based catalysts are optional for their remarkable role in vapor-phase hydrogenation, such as the hydrogenation of esters to alcohols and glycerol to propanediols.¹⁶⁻²² Cu based catalysts are effective for the chemoselective hydrogenation of C-O bonds, while fairly deficient for the hydrogenolysis of C-C bonds.²⁰ Previous studies for catalytic vapor-phase hydrogenation show that silica-supported copper catalysts are

^a State Key Laboratory of Chemical Engineering, School of Chemical Engineering, East China University of Science and Technology, 130 Meilong Road, Shanghai 200237, P. R. China. Email: liweil@ecust.edu.cn; Tel: +86-21-64253118.

^b Shanghai Pujing Chemical Industry Co. Ltd, 1305 Huajing Road, Shanghai 200231, P. R. China.

ARTICLE

Journal Name

active for di-esters to di-alcohols, like dimethyl oxalate (DMO) to ethyl glycerol (EG),^{23,24} dimethyl maleate to 1,4-butanediol²⁴⁻²⁶. Furthermore, the nature of active sites in carbonyl hydrogenation has been intensively investigated. For instance, in an earlier study, San et al.²⁷ considered Cu⁰ species to act as the only active centers in the hydrogenation process. Moreover, the synergetic effect between Cu⁰ and the oxide components has been proposed to improve the catalytic performance toward the hydrogenation of methyl acetate (MA),²⁸ dimethyl oxalate (DMO),^{29,30} furfural,^{31,32} and CO₂.³³ Although the cooperation of Cu⁰ and Cu⁺ species in C=O hydrogenation has been suggested, their respective contribution to the catalytic activity remains debated. Inspired by the known regioselectivity for Cu/SiO₂ in catalytic hydrogenation, we have adopted a homogeneous deposition precipitation method using urea as precipitator to prepare Cu/SiO₂ catalyst for DMM hydrogenation to 1,3-PDO. Such a protocol can effectively disperse Cu species on silica by forming strong metal-support interactions, thereby guaranteeing the co-existence of both Cu⁰ and Cu⁺ species in the reduced catalysts.^{23,34} The purpose of this study is to explore the catalytic hydrogenation of DMM to 1,3-PDO on Cu/SiO₂ to understand how the reaction proceeds and what constitute the active sites. A reaction network for DMM hydrogenation on Cu/SiO₂ catalysts will be proposed and the formation and nature of active sites will be explored. The effects of copper loading will also be estimated by taking advantage of a systematic characterization on the physicochemical properties of these catalysts by X-ray diffraction, Fourier transform infrared spectroscopy, H₂-temperature programmed reduction, X-ray photoelectron spectroscopy, N₂ physisorption, CO chemisorption, N₂O titration, and transmission electron microscopy. The catalysis-structure relationship will be proposed by correlating of catalyst activity to distinct curious species.

2. Experimental

2.1 Catalyst Preparation

All Cu/SiO₂ catalysts were prepared by urea-assisted deposition-precipitation (UDP) of metal nitrate salts in the presence of colloidal silica, as described previously.³⁵ Briefly, 25 wt.% colloidal silica (JA-25, Qingdao Haiyang Chemical Ltd.) was dispersed in a given amount of aqueous solution containing Cu(NO₃)₂·3H₂O (AR, Shanghai Lingfeng Chemical Reagent Co. Ltd.) and urea (A.R., Shanghai Lingfeng Chemical Reagent Co. Ltd.) in a round-bottomed flask. The suspension was then heated to 363 K under vigorously stirring, allowing a steady and homogeneous increase of pH value by the hydrolysis of urea which triggered the precipitation of a fine copper species on silica. After reaching pH 6~7, the lump was collected after hot filtration of the obtained precipitation, which was washed thrice with deionized water, dried overnight at 393 K, and calcined in air at 723 K for 4h. The

resultant catalyst precursor was denoted as xCu/SiO₂, where x stands for the preset mass loading of copper. The catalyst was crushed to sieve 40-60 mesh for the activity test in DMM hydrogenation to 1, 3-PDO.

For comparison, a reference catalyst containing 20 wt. % copper was prepared by incipient wetness of silica support with an aqueous solution of Cu(NO₃)₂·3H₂O, followed by drying (393K, 12h), and calcination at 723 K for 4 h in flowing air. The catalyst was denoted as 20Cu/SiO₂-IM.

2.2 Characterization Techniques

The actual copper amount in the samples was determined by elemental analysis using an inductively coupled plasma atomic emission spectrometer (ICP-AES, Perkin Elmer Optima 7300 DV).

XRD measurements were carried out using a Rigaku C/max-2500 diffractometer employing the graphite filtered Cu K α radiation ($\lambda=1.5406 \text{ \AA}$) with a scanning angle (2θ) range of 10-80°. The average diameter of Cu particles was calculated on the basis of the Cu⁰ (111) peak broadening according to Scherrer equation (after subtracting the instrumental broadening).

The Fourier-transform infrared (FT-IR) spectra of catalyst precursors and CO chemisorption on reduced catalysts were collected on a Nicolet 6700 spectrometer. Briefly, the samples were finely grounded, dispersed in KBr, and pelletized. The spectral resolution was 4 cm⁻¹, and 64 scans were recorded for each spectrum. For CO-chemisorption IR experiments, 30 mg of catalyst was compressed into a self-supporting wafer and reduced in a flow of 10% H₂-90%Ar (30 ml min⁻¹) at 623 K for 4 h before evacuating for 1h to remove the chemisorbed surface contaminants and cooling down to room temperature. Next, the reduced sample was exposed to highly pure CO (99.999%) for 30 min and evacuated for 30 min.

X-ray photoelectron spectroscopy (XPS) and Auger electron spectroscopy (XAES) measurements were performed on a Quantum 2000 Scanning ESCA Microprobe instrument (Physical Electronics) equipped with an Al K α X-ray radiation source ($h\nu = 1486.6 \text{ eV}$). The reduced catalyst was carefully collected and sealed under the protection of Ar after reduction. Binding energies were calibrated using the C1s peak at 284.8 eV as a reference with an uncertainty of $\pm 0.2 \text{ eV}$.

The H₂ temperature-programmed reduction (TPR) measurements were operated on a Micromeritics Autochem II 2920 instrument. Typically, catalyst of 100 mg was dried at 473K under argon (highly pure, 99.999%) (30 ml·min⁻¹) for 1 h, then cooled down to room temperature in pure argon. After that, the catalyst was then heated in 30 ml·min⁻¹ of 10%H₂-90% Ar at a ramp of 10 K·min⁻¹ up to 973 K. The amount of H₂ consumed was monitored by a thermal conductivity detector (TCD). The specific surface area of metallic copper and copper dispersion of the catalysts were determined by N₂O titration on a Micromeritics Autochem II 2920, following a method reported before.³⁶ Briefly, after pretreatment with He at 473 K for 1 h, 100 mg of the catalysts was reduced under a flow of 10 vol. % H₂/Ar (30 ml min⁻¹), and the temperature was raised from room temperature to 623 K with a ramp of 10 K min⁻¹

then cooled to 323 K. The pure N_2O (30 ml min^{-1}) was charged to the catalyst at 323 K for 0.5 h to oxidize surface Cu^0 into Cu_2O . A subsequent reduction of surface Cu_2O to Cu^0 by H_2 was conducted, and the temperature was raised to 773 K with a ramp of 10 K min^{-1} . The consumed amount of hydrogen was valued by subtracting the amount of residual H_2 calculated from the areas shown in TCD signals from the total amount of H_2 pulsed. From that, the surface metallic copper areas of catalysts could be calculated. In combination with the Cu loading measurements from ICP, the metallic Cu dispersion can be obtained as well.

N_2 adsorption-desorption analysis was conducted at 77 K employing a Micromeritics ASAP 2020 Analyzer instrument. Pore size distribution was evaluated from the desorption branches of the adsorption-desorption isotherms by the Barrett-Joyner-Halenda (BJH) method, and the specific surface area (S_{BET}) was calculated using the Brunauer-Emmet-Teller (BET) method.

Transmission electron microscopy (TEM) micro-images and High angle annular dark field scanning transmission electron microscopy (HAADF-STEM) were obtained on a JOEL JEM-2100F system electron microscope equipped with a field emission electron gun with the operation voltage of 200 kv. To prepare an appropriate sample for TEM observation, catalyst powder was ultrasonically dispersed in absolute ethanol at room temperature for 30 min and transferred onto nickel grid by dipping.

2.3 Evaluation of the Catalytic Performance

The catalytic performance was assessed in a continuous fixed-bed microreactor. Samples (40-60 mesh, 2.0 g in all cases) were packed into the tubular reactor with an inner diameter of 10 mm. The catalyst samples were pre-reduced in H_2 at 623 K for 4 h with a ramping rate of 2 K min^{-1} , and cooled to the preset reaction temperature. Afterwards, 15 wt. % DMM/methanol solution and H_2 were fed into the reactor. Typical test conditions were set to reaction temperature of 463 K, a total pressure of 5.0 MPa, and H_2 /DMM molar ratio of 200, and the weight liquid hourly space velocity of DMM ($LHSV_{DMM}$) of $0.4 \text{ g}_{cat}^{-1} \text{ h}^{-1}$. The products were condensed with a cold trap, collected and then analyzed using a Huaai GC 9560 with DB-200 capillary column and a flame ionization detector (FID). The major byproducts include methanol, methyl acetate, n-propanol, methyl propionate, and methyl 3-hydroxypropionate.

3. Results

3.1 XRD patterns

The Cu/SiO_2 catalysts with varied Cu loadings were prepared following a previously established homogeneous precipitation UDP method.³⁵ Fig. 1(A) illustrates the XRD profiles for the calcined xCu/SiO_2 precursors prepared from UDP protocol and a contrast $20Cu/SiO_2$ -IM sample derived from an impregnation method. The XRD patterns of all the UDP derived samples exhibited an amorphous pattern except $40Cu/SiO_2$, no obvious diffraction peak of bulky CuO or related cupreous substances

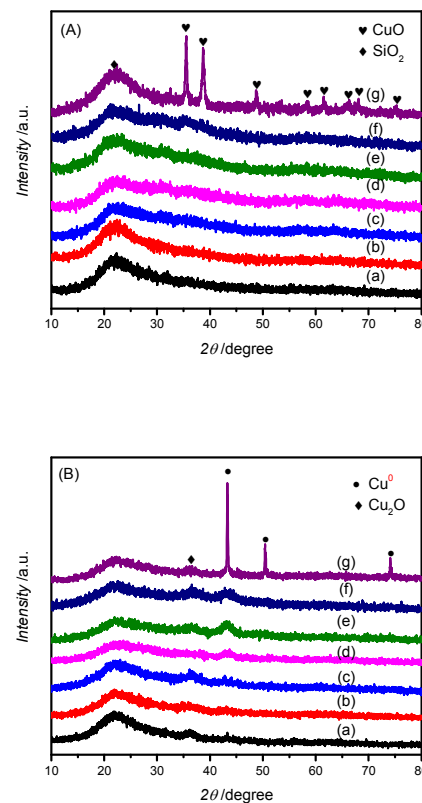


Fig. 1. XRD patterns of Cu/SiO_2 catalysts: (a) $10Cu/SiO_2$, (b) $15Cu/SiO_2$, (c) $20Cu/SiO_2$, (d) $25Cu/SiO_2$, (e) $30Cu/SiO_2$, (f) $40Cu/SiO_2$, (g) $20Cu/SiO_2$ -IM.

could be observed in all the samples, indicating the formation of highly dispersed amorphous copper species at low loadings.²⁹ Weak reflections at 35.4° and 38.7° from CuO (tenorite) (JCPDS 05-0661) can be observed for $40Cu/SiO_2$, showing copper oxide agglomerated at this loading. In striking contrast, the $20Cu/SiO_2$ -IM consists of well-developed CuO , as exhibited by the sharp diffractions in Fig. 1(A). The diffraction lines of CuO for UDP-derived catalysts are less intense and much broader than the $20Cu/SiO_2$ -IM, indicating that UDP is advantageous in promoting the metal dispersion in precursors. The broad feature at 2θ of approximately 22° from amorphous silica support. The enhanced dispersion of copper in the catalyst precursors is reckoned as a result of formation of copper phyllosilicate phase (JCPDS 00-003-0219), which has been identified by the diffraction peaks at 2θ of 31.0 , 34.8 , 57.2 , 63.3 , and 71.2° (Supporting Information, Fig. S1). It also should be noted that the peaks from copper phyllosilicate diminished without notable development of the peaks from copper oxide after calcination (Fig. S1). Consequently, a well dispersed CuO on the calcined Cu/SiO_2 samples can emerge as a result of copper phyllosilicate thermal decomposition. The phenomenon could arise from the preparation method, as homogeneous precipitation favors complexing of Cu^{2+} with the

surface silanols by forming $=\text{SiOCu}_n$ monomers and their subsequent polymerization leads to the formation of phyllosilicate.^{24,35,37,38} Toupance et al.³⁹ found that a fraction of copper phyllosilicate tends to decompose during calcination at 723 K. Van der Grift et al.⁴⁰ also revealed that a fraction of copper phyllosilicate decomposes when calcined, bringing about well dispersed CuO accompanied by the intact copper phyllosilicate.

After reduction (Fig. 1(B)), the Cu/SiO₂ catalysts demonstrate an obvious diffraction peak at 2θ of 43.3° along with two weak ones at 50.4 and 74.1°, which are characteristics of Cu (110) (JCPDS 04-0836).²⁹ The intensity of these diffraction lines grow with Cu contents in the UDP-derived samples, and becomes only visible at loadings higher 25 wt.%. Below this loading, no obvious diffraction peak can be observed, indicating that the Cu is well dispersed and does not form crystalline structure to be detected by XRD technique. Apart from that, a broad and weak peak at 36.4° which is ascribable to the Cu₂O (111) plane (JCPDS 05-0667),⁴¹ is presented in the high-loading reduced catalysts. These findings show that the Cu⁰ and Cu₂O coexist in the functioning catalysts. Unlike samples derived from UDP protocol, copper species aggregated to larger clusters (*ca.* 34.2 nm) after reduction in the 20Cu/SiO₂-IM catalyst, due to its weak interaction with the silica support and the aggregation of metallic copper.⁴² In short, XRD results demonstrate that UDP-derived sample are made up of well dispersed Cu species on SiO₂ support, owing to the strong interaction between the Cu²⁺ with Si-OH on silica surface that lead to the formation of a precursor copper phyllosilicate. Partial reduction of copper phyllosilicate in H₂ atmosphere produces metallic Cu species together with Cu₂O in the silica matrix.

3.2 Fourier-transform infrared spectroscopy (FTIR)

Fourier-transform infrared spectroscopy (FTIR) has been used to detect the formed species in catalyst preparation, as displayed in Fig. 2. FTIR is employed to probe copper phyllosilicate (Cu₂Si₂O₅(OH)₂), because the fingerprint δ_{OH} bands in the structure are clearly distinguishable.^{35,43} The broad adsorption bands centered at approximately 3460 cm⁻¹ in the spectra for calcined samples (Fig. 2(A)) are attributed to the OH stretching vibration of water and surface silanols.⁴⁴ Similarly, the bands around 1630 cm⁻¹ are ascribed to the bending mode of OH groups of adsorbed water.⁴⁴ Bands at approximately 1110 cm⁻¹ are ascribed to stretching vibration of Si-O bond; bands at 800 and 470 cm⁻¹ are associated with bending vibration modes of the Si-O bond in amorphous silica.⁴⁵ The δ_{OH} vibration at 670 cm⁻¹ together with the $\nu_{\text{Si-O}}$ shoulder peak at 1040 cm⁻¹ suggests that the existence of copper phyllosilicate³⁵ in the calcined samples derived from UDP method. In contrast, such features are not detected for the 20Cu/SiO₂-IM sample, showing that no copper phyllosilicate is produced by impregnation method. Weak vibration bands at 575, 500, and 460 cm⁻¹ belonging to CuO phase^{46,47} (Fig. 2(A)) have not been observed, as the intense and broad band at 470 cm⁻¹ from silica overlaps with them. The relative amount of copper phyllosilicate in the calcined Cu/SiO₂ catalysts can be evaluated by I_{670}/I_{800} ³⁵ which is

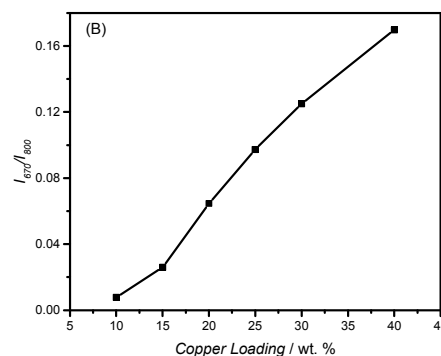
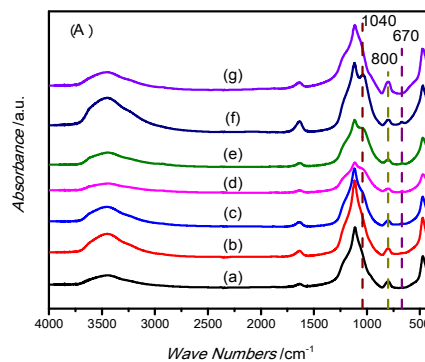


Fig. 2. (A) FTIR spectra of calcined samples with different copper loadings. (B) The I_{670}/I_{800} intensity ratio. (a) 10Cu/SiO₂, (b) 15Cu/SiO₂, (c) 20Cu/SiO₂, (d) 25Cu/SiO₂, (e) 30Cu/SiO₂, (f) 40Cu/SiO₂, (g) 20Cu/SiO₂-IM.

defined as the ratio between the integrated intensity of the δ_{OH} band at 670 cm⁻¹ and the integrated intensity of the $\nu_{\text{Si-O}}$ symmetric stretching band of SiO₂ at 800 cm⁻¹. The I_{670}/I_{800} ratio gives semi-qualitative amount of copper phyllosilicate, as the extinction coefficients of the corresponding IR bands are not known. Fig. 2(B) demonstrates the relative amount of copper phyllosilicate in calcined Cu/SiO₂ samples as a function of copper loading. The copper phyllosilicate content is found to increase with increasing Cu loading for samples derived from UDP method, whereas no copper phyllosilicate is detected for impregnated sample 20Cu/SiO₂-IM, which is in line with XRD result.

The structural evolution during catalyst preparation for a representative 20Cu/SiO₂ is shown in Fig. S2. Copper phyllosilicate is only detectable for as-prepared and calcined samples, and H₂ reduction has caused its complete decomposition.

3.3 H₂-TPR profiles of the calcined catalysts

H₂-TPR has been applied to characterize reducibility of calcined catalysts to obtain some surface species information. TPR profiles (Fig. 3) of all the UDP-derived catalysts present a single reduction peak centered at *ca.* 483 K. This reduction pattern can be attributed to the presence of well dispersed Cu²⁺

species with small particle size (< 10.5 nm), according to previous assignment.⁴⁸ The absence of reduction peaks below 473 K and 528-573 K suggests the lack of copper oxocations (Cu-O-Cu)²⁺^{49,50} and bulk copper oxide,⁵¹⁻⁵³ respectively. Unlike UDP-derived samples, there are three adjacent reduction peaks can be identified, with reduction temperatures centered at 470, 500, and 560 K, belonging to the reduction of CuO with diverse sizes. The 470 and 500 K temperature reduction peaks are often ascribed to the reduction of fine CuO nanoparticles, whose varied size can cause the divergence of reduction temperature. The reduction at 560 K is generated by the reduction of bulky CuO.⁵⁴ The presence of bulky CuO phase is also confirmative to the XRD pattern for the same sample (Fig. 1(A)). As the reduction of well dispersed CuO to Cu⁰ occurs at the same temperature for copper phyllosilicate reduction to Cu⁺, the two species cannot be differentiated by using H₂-TPR.^{42,50} Briefly, H₂-TPR measurements demonstrate that samples derived from UDP method comprise mainly well dispersed Cu species, whereas impregnation-derived sample with both dispersed and bulk CuO.

3.4 XPS measurements

To elucidate the chemical states of the copper species in the reduced samples, surface sensitive XPS and AES spectra have been collected, as manifested in Fig. 4. To exclude the adventitious oxidation of Cu⁰ by contacting with air, the as-reduced samples were sealed in protection of N₂ before measurements. For the reduced samples (Fig. 4(A)), the binding energy of Cu 2p_{3/2} core levels appearing at 932.4 - 932.9 eV could be attributed to either Cu⁺ or Cu⁰.⁵⁵ In the case of Cu 2p_{3/2}, there should be one main peak at ca. 935.8 eV, with an accompanied satellite lines.²⁴ The absence of these characteristics imply that no Cu²⁺ presents in the reduced samples derived from UDP method. The discrimination was also verified by the presence of Cu₂O and Cu phases found in XRD measurements at high loadings (Fig. 1(B)). To determine

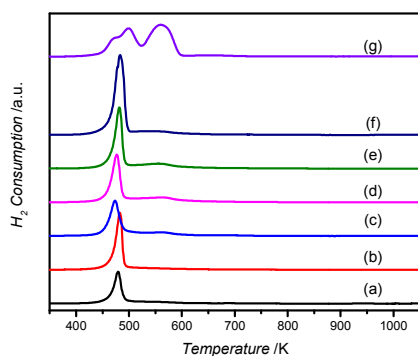


Fig. 3. TPR profiles of the Cu/SiO₂ catalysts. (a) 10Cu/SiO₂, (b) 15Cu/SiO₂, (c) 20Cu/SiO₂, (d) 25Cu/SiO₂, (e) 30Cu/SiO₂, (f) 40Cu/SiO₂, (g) 20Cu/SiO₂-IM.

the structure change during H₂ reduction, the XPS patterns for typical as-prepared and reduced 20Cu/SiO₂ are laid out in Fig.

S3. The Cu 2p_{3/2} peak at 935.7 eV with a shoulder on the high BE side, is characteristic of Cu²⁺ species^{34,56} in the calcined samples. The asymmetry of Cu 2p_{3/2} envelope allows the calcined sample peak to be deconvoluted into two contributions entering around 933.4 and 935.9 eV, corresponding to well dispersed CuO and copper phyllosilicate, respectively.^{51,57} Therefore, the rather large positive shift of the Cu2p binding energy implies that the charge from the metal ions transfer toward the support matrix, meaning that the metal ions interact with the support rather strongly.⁵⁸ Apparently, the co-existence of copper phyllosilicate and well dispersed CuO contribute to the observed asymmetric line-shape of the Cu 2p_{3/2} peaks of the samples in Fig. S3, which is in line with the XRD, FTIR results.

In order to discriminate Cu⁰ and Cu⁺ species, which are nearly identical in their XPS patterns, AES spectra are measured (Fig. 4(B)).⁵⁵ It is clear that each Cu LMM spectrum involves multiple components as indicated by the asymmetric and broad shape for the LMM peak. The broad envelope can be deconvoluted into two individual peaks centered at 916.0 and 912.0 eV, corresponding to Cu⁰ and Cu⁺, respectively.²⁴ Henceforth, there coexists Cu⁰ and Cu⁺ species on silica-supported copper catalysts derived from UDP protocol.²³

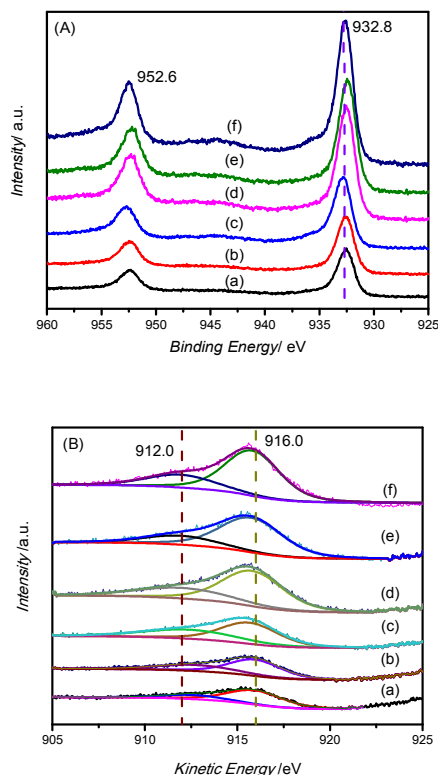


Fig. 4. (A) Cu 2p XPS spectra of the reduced catalysts; (B) Cu LMM XAES profiles of the reduced catalysts with different copper loadings. (a) 10Cu/SiO₂, (b) 15Cu/SiO₂, (c) 20Cu/SiO₂, (d) 25Cu/SiO₂, (e) 30Cu/SiO₂, (f) 40Cu/SiO₂.

ARTICLE

Journal Name

Table 1 Cu LMM deconvolution results of the surface Cu components in the reduced catalysts

Sample	KE (eV) ^a		AP (eV) ^b		Cu 2p _{3/2} BE (eV)	X _{Cu⁺} (%) ^c
	Cu ⁺	Cu ⁰	Cu ⁺	Cu ⁰		
10Cu/SiO ₂	913.2	916.5	1845.8	1849.2	932.6	24.3
15Cu/SiO ₂	913.4	916.5	1846.0	1849.1	932.6	35.7
20Cu-SiO ₂	913.0	916.2	1845.7	1848.9	932.8	41.0
25Cu-SiO ₂	912.6	916.4	1845.2	1849.0	932.6	31.4
30Cu-SiO ₂	912.9	916.5	1845.3	1848.9	932.5	30.1
40Cu-SiO ₂	912.5	916.3	1845.1	1849.0	932.7	26.3

Note: ^a Kinetic Energy. ^b Modified Auger Parameter. ^c Intensity ratio between Cu⁺ and (Cu⁰ + Cu⁺) by deconvolution of Cu LMM XAES spectra.

Table 2 Characterization of Cu Species on reduced Cu/SiO₂ catalysts

Sample	S _{Cu⁰} /m ² g ^{-1a}	X _{Cu⁺} /% ^b	S _{Cu⁺} /m ² g ^{-1c}	A _{Cu⁺} /area g ^{-1d}
10Cu/SiO ₂	21.6	24.3	6.9	62
15Cu/SiO ₂	26.0	35.7	14.4	145
20Cu/SiO ₂	32.6	41.0	22.7	190
25Cu/SiO ₂	30.0	31.4	13.7	126
30Cu/SiO ₂	26.5	30.1	11.4	111
40Cu/SiO ₂	24.3	26.3	8.7	79

Note: ^a Metallic Cu surface area determined by N₂O titration. ^b Cu⁺/(Cu⁺+Cu⁰) calculated from Cu LMM XAES spectra. ^c Cu⁺ surface area estimated on the basis of S_{Cu⁰} and X_{Cu⁺} under the assumption that the Cu⁺ ions and Cu⁰ atoms occupy identical areas and have identical atomic sensitivity factors. ^d Integral area under the peaks of CO adsorption on active Cu⁺ on the surface of catalysts after evacuation (Figure S4).

An influence of the copper loading on the components of the Cu⁺ and Cu⁰ species could be inferred from AES measurement. Table 1 compiles the deconvolution results of the original Cu LMM peaks, as well as the peak positions and their distinct contributions. The Cu⁺ / (Cu⁺ + Cu⁰) ratio collected from the deconvolution of Cu LMM spectra increased with the copper loading, and passes a maximum at 20 wt.% with a ratio of 41.0%. It has been recognized that CuO weakly bonding to the support can be readily reduced to Cu⁰ at 513 K.^{59,60} It is reckoned that the strong metal-support interaction in Cu²⁺-SiO₂ has hindered the complete reduction of Cu²⁺ into Cu⁰, and henceforth some Cu⁺ has formed after H₂ reduction. At high Cu loadings, the formation of excessive CuO phase results in the formation of more Cu⁰.

The modified Auger parameter α' , defined as the summation of the kinetic energy (KE) of the Cu LMM Auger electron and the binding energy of the Cu 2p_{3/2} photoelectron, was performed to quantify the contribution from Cu⁰ and Cu⁺ species.⁵¹ Generally, α' is ca. 1851.0 eV for Cu⁰ and 1849.0 eV for Cu⁺.⁶¹ In addition, it can be 2-3 eV lower when the copper (in +2, +1, or 0 valence) is highly dispersed and interacts intimately with the support.⁶² Therefore, as demonstrated in Table 2, the α' values at ca. 1849.0 eV and ca.

1846.0 eV can be attributed to Cu⁰ and Cu⁺, respectively. The smaller α' for Cu⁰ and Cu⁺ than the bulk values stem from the highly dispersed state and the strong interaction with silica, respectively. In short, the strong metal-support interaction leads to the partial reduction precursor and co-presence of both Cu⁰ and Cu⁺ species.

3.5 TEM images

Fig. 5 demonstrates the HRTEM images of the representative 20Cu/SiO₂ samples after calcination and reduction. The HRTEM images clearly reveal that numerous whisker-shaped copper phyllosilicate are present in the calcined sample, and no obvious CuO particles can be observed since they are either well dispersed or incorporated into silica substrate. After reduction at 623 K, the whisker-shaped copper phyllosilicate vanished, with the formation of Cu⁰ (< 5nm in size) densely covering the surface of the cross-linked SiO₂ spheres. In addition, surface characterization by HAADF-STEM was also used to determine the surface distributions of Cu species on the Cu/SiO₂ catalyst (Fig. 5(D)), demonstrating that via urea-assisted deposition precipitation, the Cu species are evenly distributed onto the silica texture. Fig. S5 compares the representatives for the IM- and UDP-series of the calcined and reduced samples. As for the IM-derived one, copper particles can be clearly observed on the silica surface without any whisk-like phyllosilicate after calcination, and they aggregated resulting a poorer copper dispersion after reduction at 623 K. For the calcined UDP- samples, the corresponding amount of copper phyllosilicate with the increase in copper loading can be directly observed. This agrees well with the FTIR observation that content of

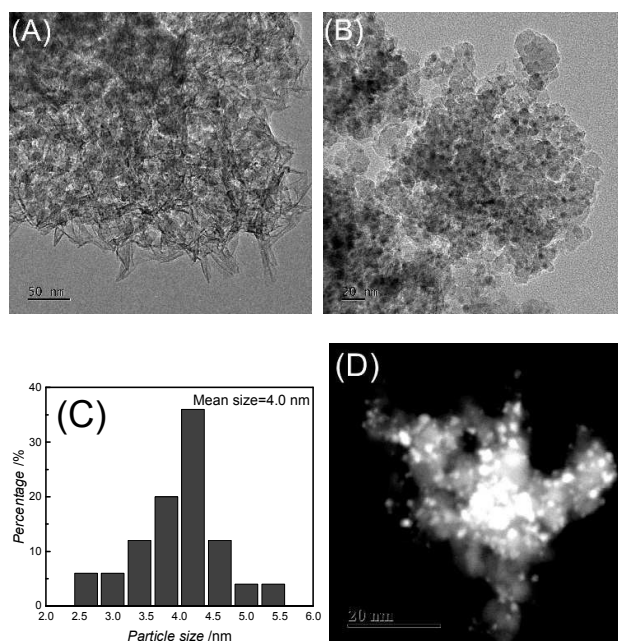


Fig. 5. HRTEM images of 20Cu/SiO₂: (A) as-calcined; (B) as-reduced; (C) particle size distribution of the as-reduced catalyst; (D) HAADF-STEM image of the as-reduced catalyst.

phyllosilicate grows with the copper loading, as demonstrated by the I_{670}/I_{800} ratio increase with increasing Cu loading. For the reduced catalysts, the sizes of copper particles are notably small (<5 nm), which is consistent with the estimation using Scherrer's equation (Table 3). Besides, the TEM images shows that copper is well dispersed on support for all the reduced catalysts, and is confirmative to absence of XRD diffraction lines.

3.6 N₂O titration

The exposed active surface areas for metallic Cu⁰ has been deduced from a N₂O titration measurements, as is compiled in Table 3. The metallic copper surface area increases through a maximum of 32.6 m² g⁻¹ at the copper loading of 20 wt. %, then decreases to 26.5 m² g⁻¹. In contrast, the Cu⁰ surface area of 20Cu/SiO₂-IM is 3.4 m² g⁻¹. The efficacious dispersion of copper species on the catalyst surface can be ascribed to the special textural structure originating from that copper phyllosilicate.

3.7 Physicochemical properties of catalyst

Textural properties have been derived from N₂ adsorption branch of the physisorption isotherms, as shown in Fig. 6. The physicochemical properties of the calcined Cu/SiO₂ samples are tabulated in Table 3. Fig. 6(A) and Fig. 6(B) demonstrates the N₂ adsorption-desorption isotherms and the corresponding pore size distribution curves of the calcined samples, respectively. It is found that the BET surface area increased from 287 to 422 m² g⁻¹ when the copper loading increases from 5 to 25 wt.%, then decreases to 388 m² g⁻¹ when copper loading further increases. All these samples display type IV isotherms, and the abrupt uptake of N₂ at relative pressure of P/P_0 at 0.8 originates from a capillary effect due to the presence of mesopores. The inferred pore-size-distribution is shown in Fig. 6(B), and mesopores centered at nm can be derived, showing that UDP method could create a porous matrix during preparation. The pore size distribution curves

derived from the desorption branch using the BJH algorithm (Fig. 1B) show that at elevated copper loadings, the contribution of pores at ca. 12.4 nm to the total pore volume increased considerably at the expense of pores at ca. 7.6 nm. The appearance of the larger pore sizes and improvements of BET surface area in the calcined samples may originate from the abundant formation of copper phyllosilicate which is reported to enhance the BET surface area,⁴⁸ whose formation is also confirmed by FTIR and TEM. On account of the fact that the copper content in the precipitates never exceeded that of bulk chrysocolla (ca. 40 wt. %), all copper species in the catalyst precursors could be accommodated in a well-dispersed state,⁴⁸ which has been identified by XRD, XPS, and TEM. The hysteresis loops vary from H1-type for 20Cu/SiO₂ to H3 type for 25Cu/SiO₂ implying that the pore shapes of these Cu/SiO₂ samples have altered from spherical to silt-like channels.⁶³ The hysteresis loop demonstrated in Fig. 6(A) is typically acquired with aggregated platy particles with slit-shaped mesopores,³⁰ which is corroborated also by the TEM images (Fig. S5).

3.8 Catalytic tests

The catalytic performance of the above prepared catalysts was pre-reduced in H₂ before catalytic DMM hydrogenation tests. The tests were carried out at 463 K, 5.0 MPa, LHSV_{DMM} 0.4 g g_{cat}⁻¹ h⁻¹, DMM/H₂ molar ratio 200, in a fixed bed reactor. Besides 1,3-PDO, sides products, such as methyl 3-hydroxypropionate (3-HPM), n-propanol (NPA), methyl propionate (MP), and methyl acetate (MA) are also detected in the products. Catalytic activity and selectivity as a function of Cu loading are shown in Fig. 7. The catalytic activity in terms of DMM conversion is found to increase hand-in-hand with Cu loading, but more significant at loadings below 20 wt.%. Above 20 wt.%, the conversion reaches > 90% and increase in activity becomes less prominent with Cu loading increase. The

Table 3 Physicochemical properties of the UDP-derived Cu/SiO₂ catalysts compared with 20Cu/SiO₂-IM catalyst

Catalyst	Cu loading ^a (wt. %)	S _{BET} (m ² g ⁻¹)	V _p (cm ³ g ⁻¹)	D _p (nm)	D _{Cu} (%)	S _{Cu⁰} (m ² g ⁻¹)	Metallic Crystallite size (nm) ^b		TOF _{DMM} ^d (h ⁻¹)
							by XRD ^c	by N ₂ O titration	
10Cu/SiO ₂	9.8	287	0.50	7.0	33.3	21.6	ND ^c	3.2	2.4
15Cu/SiO ₂	14.7	313	0.57	7.2	26.7	26.0	ND	4.0	3.6
20Cu/SiO ₂	19.8	361	0.78	8.6	25.1	32.6	ND	4.3	5.8
25Cu/SiO ₂	24.6	422	0.82	8.8	18.5	30.0	5.9	5.8	5.5
30Cu/SiO ₂	29.4	406	0.81	7.9	14.5	28.3	6.3	7.4	4.6
40Cu/SiO ₂	39.5	388	0.67	6.9	10.2	26.5	7.9	10.5	4.0
20Cu/SiO ₂ -IM	20.2	148	0.28	7.5	2.6	5.4	34.2	31.5	2.0

Note: ^a Determined by ICP-AES analysis. ^b Diameter of Cu particles obtained from the XRD data by the Scherrer equation. ^c ND= not detected. ^d The TOF value was calculated as moles of ester reacted in the initial 1h per mole of surface copper calculated from the copper dispersion.

Journal Name

ARTICLE

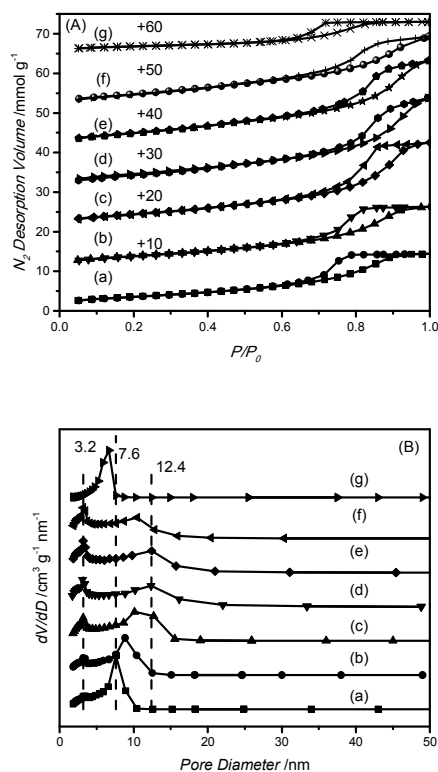


Fig. 6. (A) N₂ physisorption isotherms of the calcined catalysts; (B) BJH mesopore size distribution for the calcined catalysts. (a) 10Cu/SiO₂, (b) 15Cu/SiO₂, (c) 20Cu/SiO₂, (d) 25Cu/SiO₂, (e) 30Cu/SiO₂, (f) 40Cu/SiO₂, (g) 20Cu/SiO₂-IM.

selectivity for target product 1,3-PDO increases with Cu loading until a maximum (34.1%) is attained at 20 wt.% Cu loading, and selectivity drops with further loading increase. The 20Cu/SiO₂ catalyst demonstrated a highest activity (90.5% conversion for DMM hydrogenation) with 34.1% of 1,3-PDO selectivity. The selectivity for side-products, both methyl propionate and n-propanol increases with increasing Cu loading, with analogous trend to that of DMM conversion. The selectivity for 3-HPM is found to decrease with increasing loading and DMM conversion. Selectivity for MA is independent of Cu loading, and also remains low (< 5%) during the tests. For 20Cu/SiO₂-IM and 20Cu/SiO₂ with identical Cu loading, both higher activity and higher 1,3-PDO selectivity have been manifested by the latter, showing that UDP is the

preferred method for catalyst preparation. In contrast, the DMM conversion of 70.4% and the 1,3-PDO selectivity of 20.6% were obtained on the IM catalyst with the same copper loading. These results evidently showed the UDP catalyst is efficacious in the chemo-selective hydrogenation of DMM to 1,3-PDO, which may be ascribed to the enhanced Cu⁰ surface area (Fig. S6).

The analyses of products distribution allow the identification of the different side reactions and the mapping of the reaction network. As shown in Scheme 1, DMM hydrogenation is a consecutive reaction, according to the gas kinetic theory, the possibility of the simultaneous hydrogenation of two C=O functional groups is very low. Therefore, the main reaction of DMM hydrogenation is believed to involve two serial reactions: the hydrogenation of DMM to form methyl 3-hydroxypropionate (3-HPM) and the subsequent hydrogenation of 3-HPM to produce 1,3-PDO. Besides the hydrogenation to 1,3-PDO, 3-HPM also undergoes a parallel dehydration-hydrogenation to methyl propionate (MP) based on the hydrogenation of different functional groups in 3-HPM. Furthermore, excessive hydrogenation of both 1,3-PDO and MP can lead to the formation of n-propanol (NPA). In parallel to hydrogenation reaction, a small fraction (< 5%) of DMM decomposes to form methyl acetate (MA) and CO₂. The comparable hydrogenation selectivities for 1,3-PDO and MP

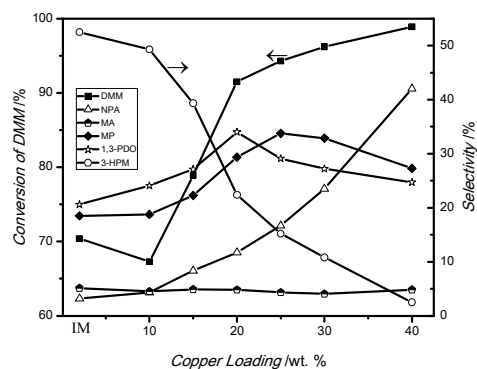


Fig. 7. Catalytic performance of Cu/SiO₂ catalyst for DMM hydrogenation as a function of copper loading. The 20Cu/SiO₂-IM sample has been shifted to 0 on the x-axis. Reaction conditions: $T=463$ K, $P=5.0$ MPa, $H_2/DMM=200$ (mol/mol), and $LHSV_{DMM}=0.4$ g_{cat}⁻¹ h⁻¹.

suggest that the two parallel reaction leading to their formation have close kinetic features. Their selectivities reach maximum at medium conversion levels, together with the continuous increase in NPA with DMM conversion, strongly suggest that both 1,3-PDO and MP are intermediates for the formation of NPA. This is for the very first time that DMM hydrogenation network has been disclosed. The finding demonstrates that future efforts should be placed on the control over catalyst hydrogenation chemo-selectivity and prevent excessive hydrogenation to unwanted NPA, and simultaneously lower the decomposition of DMM.

The influence of operation conditions, including liquid hourly space velocity of dimethyl malonate ($LHSV_{DMM}$), temperature, pressure, and H_2/DMM ratio, on DMM catalytic hydrogenation was also explored for $20Cu/SiO_2$, as displayed in Fig. 8. For a given reaction temperature (463 K), pressure (5.0 MPa), and H_2/DMM ratio (200 mol/mol), the conversion of DMM undergoes a significant decrease when increasing the $LHSV_{DMM}$ from $0.2 \text{ g}_{cat}^{-1} \text{ h}^{-1}$ to $0.6 \text{ g}_{cat}^{-1} \text{ h}^{-1}$, translating to contact variation from 0.70 min to 0.23 min. The selectivity of 3-HPM increases prominently with shorter contact

time, showing it is the primary hydrogenation product. Selectivity for 1,3-PDO and MP increases with increasing contact time, as a result of 3-HPM hydrogenation. 1,3-PDO selectivity is found to be higher than that of MP, implying that the formation of the former is kinetically favourable. Selectivity for excessive hydrogenation product, NPA, increase with contact time and exceeds selectivity for 1,3-PDO at $LHSV_{DMM}$ of $0.4 \text{ g}_{cat}^{-1} \text{ h}^{-1}$. This suggests that the longer contact time favours deeper hydrogenation, which is in consistent with the reaction network. The maximum of 1,3-PDO selectivity is obtained at $LHSV_{DMM}$ of $0.4 \text{ g}_{cat}^{-1} \text{ h}^{-1}$. Meanwhile, the selectivity for decomposition product MA is found to be unaffected by the change in contact time.

The effect of reaction temperature over the range of 443 to 483 K was also assessed, as shown in Fig. 8(B). DMM conversion increases monotonically with reaction temperature, and a simultaneous drop in 3-HPM selectivity is observed, showing a fast transformation of the reactant and primary product. The 1,3-PDO selectivity increases steadily with

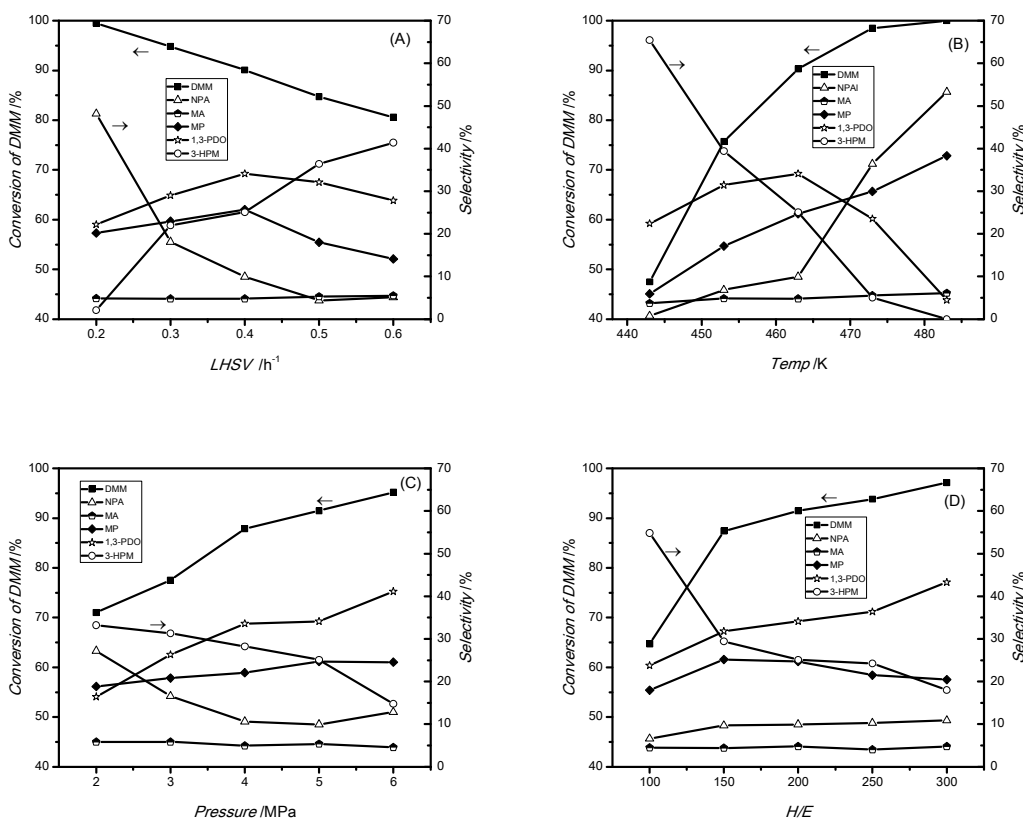


Fig. 8. Effect of reaction conditions on reaction reactivity. (A) Effect of DMM liquid hourly space velocity ($LHSV_{DMM}$), $T = 463 \text{ K}$, $P = 5.0 \text{ MPa}$, $H_2/DMM = 200 \text{ mol/mol}$. (B) Effect of temperature, $LHSV_{DMM} = 0.4 \text{ g}_{cat}^{-1} \text{ h}^{-1}$, $P = 5.0 \text{ MPa}$, $H_2/DMM = 200 \text{ mol/mol}$. (C) Effect of pressure, $LHSV_{DMM} = 0.4 \text{ g}_{cat}^{-1} \text{ h}^{-1}$, $T = 463 \text{ K}$, $H_2/DMM = 200 \text{ mol/mol}$. (D) Effect of molar ratio of H_2/DMM , $LHSV_{DMM} = 0.4 \text{ g}_{cat}^{-1} \text{ h}^{-1}$, $T = 463 \text{ K}$, $P = 5.0 \text{ MPa}$.

Journal Name

ARTICLE

temperature before passing the maximum at 463 K, whereby an optimized selectivity of 34.1% is attained. Further hydrogenation of 1,3-PDO to NPA predominates at higher temperatures. Unlike selectivity for 1,3-PDO, the MP selectivity increases with reaction temperature constantly, implying that 3-HPM dehydration-hydrogenation overrules MP hydrogenation at high temperatures. The selectivity for NPA increases with temperature, and becomes significant as a result of 1,3-PDO and MP conversion.

The DMM hydrogenation products vary significantly with pressure change for reactions involving molecule number change. Fig. 8(C) shows the corresponding selectivity for each product as a function of operating pressure. It is seen that high pressure favours the formation of 1,3-PDO, but disfavours the formation of 3-HPM and MP, reflecting that formation of 1,3-PDO is the kinetically preferred reaction at elevated pressures. It also significantly influences DMM conversion. It shows that pressure increase leads to the increase of hydrogenation products that involves a reduced molecule number, while reactions without molecular number change does not vary prominently. A high molar ratio of H_2/DMM in the feeding is also favourable for the hydrogenation of DMM, as delineated in Fig. 8(D), both DMM conversion and 1,3-PDO selectivity increase with H_2/DMM ratio under the given H_2/DMM range, and achieve their maximum of 97.1% and 43.3%, respectively at the H_2/DMM ratio of 300.

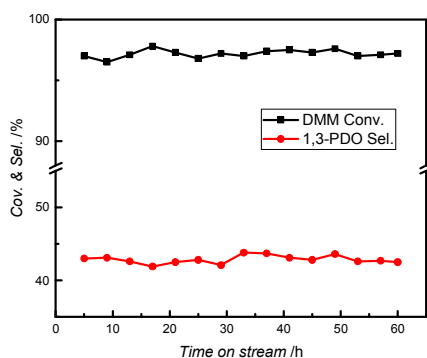


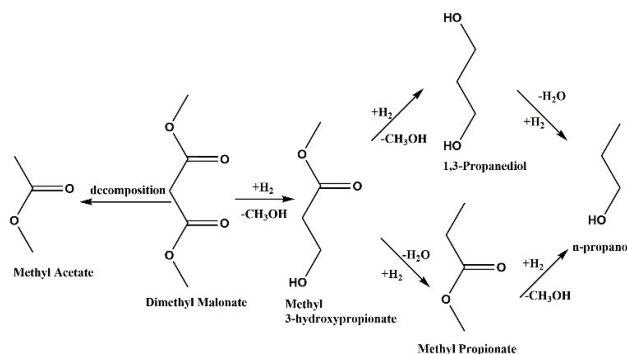
Fig. 9. The long-term catalytic performance of the DMM hydrogenation over 20Cu/SiO₂. Reaction conditions: $T = 463$ K, $P = 5.0$ MPa, $H_2/DMM = 300$, $LHSV_{DMM} = 0.4$ g_{cat}⁻¹ h⁻¹.

Among all the important chemical approaches above-mentioned, the yield is no more than 80% and 40% for AC and EO method, respectively.³ As for the glycerol hydrogenolysis method, the yield of 1,3-PDO is 28.1% (glycerol conversion 54.3%, 1,3-PDO selectivity of 52.0%),⁹ the yield of 29.3% is obtained via the hydrogenation of diethyl malonate method (90.7% conversion of dimethyl malonate, 32.3% selectivity of 1,3-PDO).^{10,11} Compared with all these approaches, the new alternative, hydrogenation of dimethyl malonate to 1,3-PDO over Cu/SiO₂, achieving a yield of 41.7%, has its promising industrial application.

The deactivation and lifespan of the Cu/SiO₂ catalysts influence the practical industrialization of vapour-phase hydrogenation of dimethyl malonate to 1,3-propanediol. Therefore, the catalytic performance of the optimal 20Cu/SiO₂ catalysts was evaluated by a time-on-stream stability test under optimal reaction conditions, i.e., 463 K, 5.0 MPa, $H_2/DMM = 300$, and $LHSV_{DMM} = 0.4$ g_{cat}⁻¹ h⁻¹ (Fig. 9). The result shows that the catalyst maintains its high catalytic activity, i.e. ca. 97% conversion of DMM and ca. 43% selectivity to 1,3-PDO, for the duration of 60 h, indicating that the 20Cu/SiO₂ catalyst exhibits a satisfactory level of catalytic activity and long-term stability under the optimal operation condition.

4. Discussion

Based on the proposed reaction network, the catalytic activity and selectivity has been correlated with Cu⁰ and Cu⁺ components in the samples (Fig. 10), with the aim to shed light on a catalysis-structure relationship. The hydrogenation activity for H₂ consumption increases almost linearly with exposing Cu⁰ surface area; the abrupt deviation to the linear relationship can be ascribed to high DMM conversion indicating too fast reaction rate of DMM hydrogenation over the catalysts under higher copper loadings (>30 wt. %), mass transfer resistance may become important and the kinetics obtained would not be intrinsic. And the yield of 1,3-PDO is in a significantly linear relationship with Cu⁰ surface area (Fig. S7), both convincing that Cu⁰ is the active site for hydrogenation reactions. This agrees well with previous reports on similar hydrogenation reaction.^{23,29,34} Deviation from linearity can be observed for the overall process may be controlled by mass transport at conversions higher than 90%. On the other hand, 1,3-PDO selectivity shows no clear trend with Cu⁰ content (Fig. S8), but increases with Cu⁺/(Cu⁺+Cu⁰) ratio (Fig. 10(B)),



Scheme 1 Catalytic reaction network for the hydrogenation of DMM over Cu/SiO₂ catalyst.

implying Cu⁺ modification is important for the selective hydrogenation to 1,3-PDO. We tentatively hypothesize that the catalytic activity is associated solely to the number of exposed surface Cu⁰, but the selectivity is strongly affected by the co-presence of Cu⁺, despite that the connection between Cu⁺ density and selectivity is still not well understood thus far. As far as the nature of active sites are concerned, there is no consensus for the hydrogenation of acyl compounds. On the one hand, some authors believe that only Cu⁰ acts as the active site, on which H₂ is dissociatively activated, and the reactant is adsorbed through the acyl group and cleaved.^{26,64} On the other hand, in methyl acetate hydrogenation, Poels and Brands,⁶⁵ Wang et al.⁵⁵ reported that the Cu⁺ sites contribute to the adsorption of methoxy and acyl species of esters, while Cu⁰ species are not capable of activating methoxy at the catalytic temperature (483 K), as sponsored by their in situ FTIR spectra and DFT modeling results. Chen et al.²⁴ also postulated that H₂ is dissociatively activated on Cu⁰ sites and the C=O bond in DMO molecules are polarized and activated on Cu⁺ sites.

In the current DMM hydrogenation, the correlations shown in Fig. 10 and Fig. S7 suggests that Cu⁰ is likely the active site where all hydrogenation reactions occur, and the Cu⁺ is crucial for the selectivity of 1,3-PDO. These speculations are supported by the XRD and AES results, as well as the clear correlation with respect to hydrogenation activity and selectivity. Cu⁺ may work as electrophilic or Lewis acidic sites to polarize the C=O bond via the electron lone pair in oxygen,⁶⁶ thus improving the reactivity of the ester group in dimethyl malonate. Thus, it is highly reasonable to suppose that Cu⁰ functions as the primary active site, and the Cu⁺ facilitates conversion of substrate and intermediates, as has been suggested in the hydrogenation reaction of dimethyl oxalate,^{34,67} dimethyl maleate,⁶⁴ furfural,⁶⁸ and crotonaldehyde.⁶⁹ Such a relationship suggests that the synergistic effect of Cu⁰ and Cu⁺ is important to the maximization of 1,3-PDO selectivity, and future efforts should

be directed towards generating and maintaining an appropriate Cu⁺/(Cu⁰ + Cu⁺) ratio for DMM hydrogenation.

5. Conclusions

In summary, dimethyl malonate vapor-phase hydrogenation to produce 1,3-PDO has been examined on Cu/SiO₂ catalyst. The catalytic hydrogenation network has been disclosed by analyzing the catalytic products distribution. Dimethyl malonate hydrogenation takes place via 3-HPM as the primary product, which can be further hydrogenated into 1,3-PDO or MP through parallel reactions. 1,3-PDO or methyl propionate can be further hydrogenated into n-propanol that reduces the selectivity of 1,3-PDO. An insignificant amount of DMM thermal decomposition can also reduce the selectivity. Manipulation of reaction temperature, pressure and feeding conditions to optimize 1,3-PDO selectivity shows that a maximized 1,3-PDO yield (41.7%) can be achieved at LHSV_{DMM} = 0.4 g g_{cat}⁻¹ h⁻¹, T = 463 K, P = 5.0 MPa, H/E = 300.

Structural characterization and catalytic performance evaluation show that co-presence of Cu⁺ is crucial for 1,3-PDO

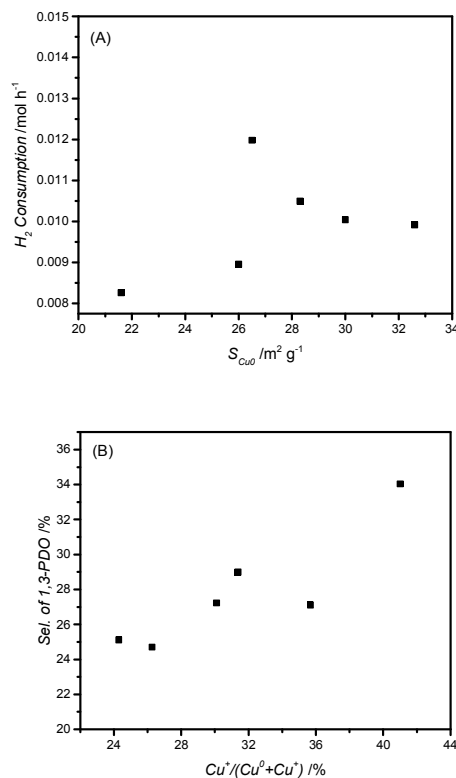


Fig. 10. Synergetic effect of Cu⁰ and Cu⁺ on the catalytic performance: (A) correlation of H₂ consumption with Cu⁰ surface areas; (B) correlation of 1,3-PDO selectivity with Cu⁺/(Cu⁰+Cu⁺)

ARTICLE

Journal Name

selectivity and Cu^0 is relevant to the overall hydrogenation activity. The reaction network and promoting role of Cu^+ are important to guide catalyst design in the future.

Acknowledgements

Support from the Research Centre of Pujing Chemical Industry Co. Ltd is gratefully acknowledged. The assistance of Yongzheng Li in performing the N_2O titration and Jingyu Zhou in performing CO-adsorption estimates is greatly appreciated.

References

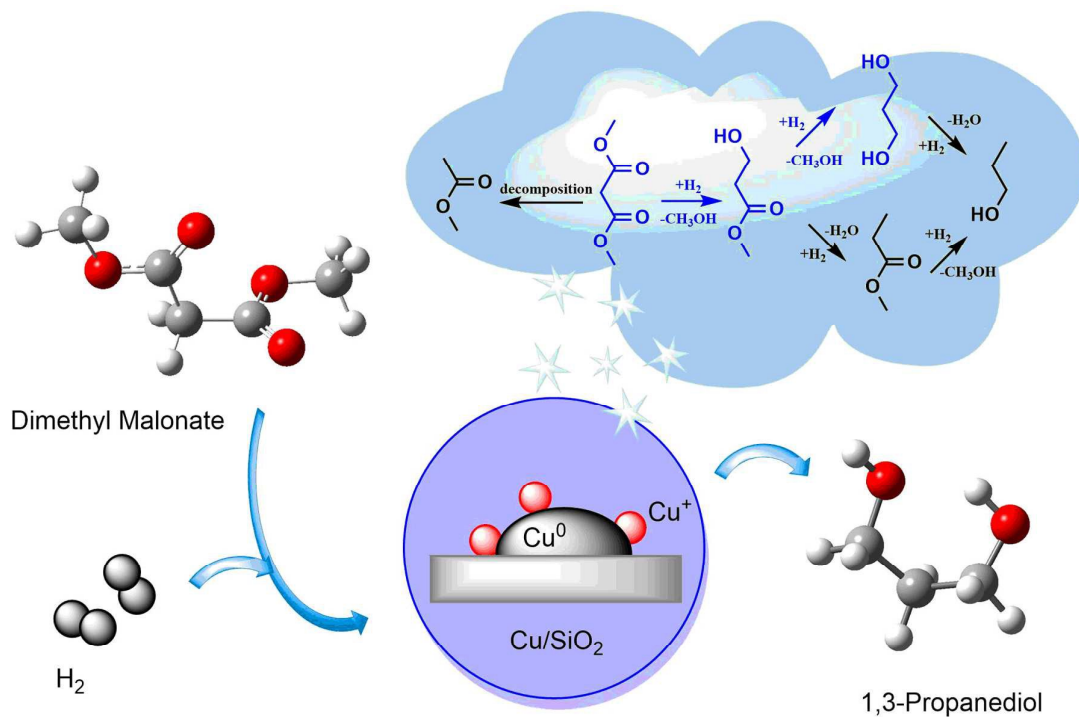
- 1 J. V., Kurian, J. Polym. Environ. 2005, **13**, 159-167.
- 2 G. A. Kraus, CLEAN - Soil, Air, Water. 2008, **36**, 648-651.
- 3 R. K. Saxena, P. Anand, S. Saran, J. Isar, Biotechnol. adv. 2009, **27**, 895-913.
- 4 H. Biebl, Appl. Microbiol. Biotechnol., 1991, **35**, 701-705.
- 5 R. A. Urban, B. R. Bakshi, Ind. Eng. Chem. Res. 2009, **48**, 8068-8082.
- 6 H. S. Wu, Y. J. Wang, Ind. Eng. Chem. Res. 2012, **51**, 10930-10935.
- 7 S. Zhu, X. Gao, Y. Zhu, J. Cui, H. Zheng, Y. Li, Appl. Catal. B. 2014, **158-159**, 391-399.
- 8 E.S. Vasiliadou, T.M. Eggenhuisen, P. Munnik, P.E. de Jongh, K.P. de Jong, A.A. Lemonidou, Appl. Catal. B. 2014, **145**, 108-119.
- 9 S. Zhu, X. Gao, Y. Zhu, Y. Zhu, H. Zheng, Y. Li, J. Catal. 2013, **303**, 70-79.
- 10 T. Ding, H. Tian, J. Liu, W. Wu, J. Yu, Chinese J. Catal. 2016, **37**, 484-493.
- 11 T. Ding, H. Tian, B. Zhao, React. Kinet. Mech. Cat. 2016, **118**, 497-508.
- 12 <http://www.grandviewresearch.com/industry-analysis/1-3-propanediol-pdo-market>
- 13 H. Yagita, H. Kuwahara, K. Omata, K. Fujimoto, ChemInform. 1990, **43**, 335-338.
- 14 K. Maeda, H. Yagita, K. Omata, K. Fujimoto, J. Mol. Catal. 1992, **71**, 347-355.
- 15 X. Wang, W. Li, R.C. Shen, Nat. Gas Chem. Ind. 2016, **41**, 38-40.
- 16 M. A. N. Santiago, M. A. Sánchez-Castillo, Cortright, R. D.; Dumesic, J. A., J. Catal. 2000, **193**, 16-28.
- 17 S. Wang, W. Guo, H. Wang, L. Zhu, S. Yin, K. Qiu, New J. Chem. 2014, **38**, 2792-2800.
- 18 J. Ding, J. Zhang, C. Zhang, K. Liu, H. Xiao, F. Kong, J. Chen, App. Catal. A-Gen. 2015, **508**, 68-79.
- 19 H. Lin, X. Zheng, Z. He, J. Zheng, X. Duan, Y. Yuan, App. Catal. A. 2012, **445-446**, 287-296.
- 20 D.S. Brands, E.K. Poels, A. Bliet, Appl. Catal. A-Gen. 1999, **184**, 279-289.
- 21 S. Zhu, X. Gao, Y. Zhu, W. Fan, J. Wang, Y. Li, Catal. Sci. Technol., 2015, **5**, 1169-1180.
- 22 Z. Huang, F. Cui, H. Kang, J. Chen, C. Xia, Appl. Catal. A. 2009, **366**, 288-298.
- 23 B. Zhang, S. Hui, S. Zhang, Y. Ji, W. Li, D.Y. Fang, J. Nat. Gas Chem. 2012, **21**, 563-570.
- 24 L. Chen, P. Guo, M. Qiao, S. Yan, H. Li, W. Shen, H. Xu, K. Fan, J. Catal. 2008, **257**, 172-180.
- 25 C. Ohlinger, B. Kraushaar-Czarnetzki, Chem. Eng. Sci. 2003, **58**, 1453-1461.
- 26 L.F. Chen, P.J. Guo, L.J. Zhu, M.H. Qiao, W. Shen, H.L. Xu, K.N. Fan, App. Catal. A-Gen. 2009, **356**, 129-136.
- 27 X.G. San, Y. Zhang, W.J. Shen, N. Tsubaki, Energy Fuel. 2009, **23**, 2843-2844.
- 28 E. K. Poels, D. S. Brands, Appl. Catal. A-Gen. 2000, **191**, 83-96.
- 29 A.Y. Yin, X.Y. Guo, W.L. Dai, K.N. Fan, J. Phys. Chem. C. 2009, **113**, 11003-11013.
- 30 S. Wang, X. Li, Q. Yin, L. Zhu, Z. Luo, Catal. Commun. 2011, **12**, 1246-1250.
- 31 K. L. Deutsch, B. H. Shanks, J. Catal. 2012, **285**, 235-241.
- 32 C. Sun, P. Zeng, M. He, X. He, X. Xie, Catal. Commun. 2016, **86**, 5-8.
- 33 S. Natesakhawat, J. W. Lekse, J. P. Baltrus, P. R. Ohodnicki, B. H. Howard, X. Deng, C. Matranga, ACS Catal. 2012, **2**, 1667-1676.
- 34 J. Gong, H. Yue, Y. Zhao, S. Zhao, L. Zhao, J. Lv, S. Wang, X. Ma, J. Am. Chem. Soc. 2012, **134**, 13922-13925.
- 35 T. Toupance, M. Kermarec, J.F. Lambert, C. Louis, J. Phys. Chem. B. 2002, **106**, 2277-2286.
- 36 E.D. Guerreiro, O.F. Gorriiz, J.B. Rivarola, L.A. Arrua, App. Catal. A-Gen. 1997, **165**, 259-271.
- 37 X. Guo, A. Yin, W.L. Dai, K. Fan, Catal. Lett. 2009, **132**, 22-27.
- 38 H. Yue, Y. Zhao, X. Ma, J. Gong, Chem. Soc. Rev., 2012, **41**, 4218-44.
- 39 T. Toupance, M. Kermarec, C. Louis, J. Phys. Chem. B. 2000, **104**, 965-972.
- 40 C. J. G. Van der Grift, A. F. H. Wielers, A. Mulder, J. W. Geus, Thermochim. Acta. 1990, **171**, 95-113.
- 41 E. D. Guerreiro, O. F. Gorriiz, G. Larsen, L. A. Arrúa, App. Catal. A-Gen. 2000, **204**, 33-48.
- 42 A.J. Marchi, L.L.G. Fierro, J. Santamaría, A. Monzón, App. Catal. A-Gen. 1996, **142**, 375-386.
- 43 Z.W. Huang, F. Cui, J.J. Xue, J.L. Zuo, J. Chen, C.G. Xia, J. Phys. Chem. C. 2010, **114**, 16104-16113.
- 44 G. Cordoba, R. Arroyo, J.L.G. Fierro, M. Viniegra, J. Solid State Chem. 1996, **123**, 93-99.
- 45 T. López, J. Hernandez-Ventura, M. Asomoza, A. Campero, R. Gómez, Mater. Lett. 1999, **41**, 309-316.
- 46 Y. X. Zhang, M. Huang, F. Li, Z. Q. Wen, Int. J. Electrochem. Sci. 2013, **8**, 8645-8661.
- 47 G. Díaz, R. Pérez-Hernández, A. Gómez-Cortés, M. Benaissa, R. Mariscal, J.L.G. Fierro, J. Catal. 1999, **187**, 1-14.
- 48 C. J. G. Van der Grift, P. A. Elberse, A. Mulder, J. W. Geus, App. Catal. 1990, **59**, 275-289.
- 49 L.Y. Chen, T. Horiuchi, T. Osaki, T. Mori, App. Catal. B-Environ. 1999, **23**, 259-269.
- 50 J.A. Anderson, C. Márquez-Alvarez, M.J. López-Munóz, I. Rodríguez-Ramos, A. Guerrero-Ruiz, App. Catal. B-Environ., 1997, **14**, 189-202.
- 51 A. Gervasini, M.M.G. Martra, A. Ponti, N.R.L. Sordelli, F. Zaccheria, J. Phys. Chem. B. 2006, **110**, 7851-7861.
- 52 C. J. G. Van der Grift, A. Mulder, J. W. Geus, App. Catal. 1990, **60**, 181-192.
- 53 Q. Sun, Y.L. Zhang, H.Y. Chen, J.F. Deng, D. Wu, S.Y. Chen, J. Catal. 1997, **167**, 92-105.
- 54 F. Boccuzzi, A. Chiorino, G. Martra, M. Gargano, N. Ravasio, B. Carrozzini, J. Catal. 1997, **165**, 129-139.
- 55 Y. Wang, Y. Shen, Y. Zhao, J. Lv, S. Wang, X. Ma, ACS Catal. 2015, **5**, 6200-6208.
- 56 G. Petrini, F. Garbassi, J. Catal. 1984, **90**, 113-118.
- 57 B. Peplinski, W. E. S. Unger, I. Grohmann, Appl. Surf. Sci. 1992, **62**, 115-129.
- 58 G. G. Jernigan, G. A. Somorjai, J. Catal. 1994, **147**, 567-577.
- 59 Z. Liu, M.D. Amiridis, Y. Chen, J. Phys. Chem. B. 2005, **109**, 1251-1255.
- 60 E. L. Rodrigues, A. J. Marchi, C. R. Apesteguía, J. M. C. Bueno, App. Catal. A-Gen. 2005, **294**, 197-207.
- 61 K. Sun, W. Lu, F. Qiu, S. Liu, X. Xu, App. Catal. A-Gen. 2003, **252**, 243-249.
- 62 M. A. Kohler, H. E. Curry-Hyde, A. E. Hughes, B. A. Sexton, N. W. Cant, J. Catal. 1987, **108**, 323-333.

Journal Name

ARTICLE

- 63 R. Schmidt, E. W. Hansen, M. Stoecker, D. Akporiaye, O.H. Ellestad, *J. Am. Chem. Soc.* 1995, **117**, 4049-4056.
- 64 M. Mokhtar, C. Ohlinger, J. H. Schlender, T. Turek, *Chem. Eng. Technol.* 2001, **24**, 423-426.
- 65 E. K. Poels, D. S. Brands, *App. Catal. A-Gen.* 2000, **191**, 83-96.
- 66 S. Sitthisa, T. Sooknoi, Y. Ma, P. B. Balbuena, D. E. Resasco, *J. Catal.* 2011, **277**, 1-13.
- 67 S. Hui, B. Zhang, S. Zhang, W. Li, *J. Nat. Gas Chem.* 2012, **21**, 753-758.
- 68 C. P. Jiménez-Gómez, J. A. Cecilia, D. Durán-Martín, R. Moreno-Tost, J. Santamaría-González, J. Mérida-Robles, R. Mariscal, P. Maireles-Torres, *J. Catal.* 2016, **336**, 107-115.
- 69 A. Dandekar, R.T.K. Baker, M.A. Vannice, *J. Catal.* 1999, **184**, 421-439.

Contents Entry



1,3-propanediol was synthesized via the hydrogenation of dimethyl malonate over Cu/SiO₂ catalyst. The reaction network and active sites were revealed for the first time.